

1 Estimation of cold plasma outflow during 2 geomagnetic storms

S. Haaland^{1,2}, A. Eriksson³, M. André³, L. Maes⁴, L. Baddeley⁵, A. Barakat⁷,
R. Chappell⁸, V. Eccles⁷, C. Johnsen⁶, B. Lybekk¹⁰, K. Li², A. Pedersen¹⁰, R.
Schunk⁷, D. Welling⁹

S. Haaland, Birkeland Centre for Space Science, University of Bergen, Norway & Max-Planck
Institute for Solar Systems Research, Göttingen, Germany (Stein.Haaland@ift.uib.no)

C. Johnsen, B. Lybekk, A. Pedersen, University of Oslo, Norway

L. Maes, Belgian Institute of Aeronomy, Brussels, Belgium

L. Baddeley, The University Centre in Svalbard, Longyearbyen, Norway

K. Li, Max-Planck Institute, Göttingen, Germany

M. André, A. Eriksson, Swedish Institute of Space Physics, Uppsala, Sweden

D. Welling, University of Michigan, Ann Arbor, MI, USA

R. Chappell, Vanderbilt University, Nashville, TN, USA

A. Barakat, R. Schunk, V. Eccles, Utah State University, Logan, UT, USA

¹Birkeland Centre for Space Science,

This is the author manuscript accepted for publication and has undergone full peer review but has not been through the copyediting, typesetting, pagination and proofreading process, which may lead to differences between this version and the Version of Record. Please cite this article as doi:

D **10.1029/2015JA021810**

November 10, 2015, 7:21pm

D R A F T

3 **Abstract.** Low energy ions of ionospheric origin constitute a significant
4 contributor to the magnetospheric plasma population. Measuring cold ions
5 is difficult though. Observations have to be done at sufficiently high altitudes

University of Bergen, Norway

²Max-Planck Institute for Solar Systems

Research, Göttingen, Germany

³Swedish Institute of Space Physics,

Uppsala, Sweden

⁴Belgian Institute of Aeronomy, Brussels,

Belgium

⁵The University Centre in Svalbard,

Longyearbyen, Norway

⁶Department of Geophysics, University of

Oslo, Norway

⁷Utah State University, Logan, UT, USA

⁸Vanderbilt University, Nashville, TN,

USA

⁹University of Michigan, Ann Arbor, MI,

USA

¹⁰Department of Physics, University of

Oslo, Norway

6 and typically in regions of space where spacecraft attain a positive charge
7 due to solar illumination. Cold ions are therefore shielded from the satellite
8 particle detectors. Furthermore, spacecraft can only cover key regions of ion
9 outflow during segments of their orbit, so additional complications arise if
10 continuous longtime observations, such as the during a geomagnetic storm,
11 are needed. In this paper we suggest a new approach, based on a combina-
12 tion of synoptic observations and a novel technique to estimate the flux and
13 total outflow during the various phases of geomagnetic storms. Our results
14 indicate large variations in both outflow rates and transport throughout the
15 storm. Prior to the storm main phase, outflow rates are moderate, and the
16 cold ions are mainly emanating from moderately sized polar cap regions. Through-
17 out the main phase of the storm, outflow rates increase and the polar cap
18 source regions expand. Furthermore, faster transport, resulting from enhanced
19 convection, leads to a much larger supply of cold ions to the near Earth re-
20 gion during geomagnetic storms.

Author Manuscript

1. Introduction

21 Ions of ionospheric origin are believed to be a significant contributor to the magneto-
22 spheric plasma population [*Shelley et al.*, 1982; *Horwitz*, 1982; *Chappell et al.*, 1987, 2000;
23 *André and Cully*, 2012]. Major ionospheric outflow regions include the auroral zone [e.g.,
24 *Wahlund and Opgenoorth*, 1989; *Winser et al.*, 1989; *Yau et al.*, 1993; *André et al.*, 1998;
25 *Wilson et al.*, 2001] the cusp [e.g., *Yau et al.*, 1985b; *Lockwood et al.*, 1985b, a; *Yau and*
26 *Andre*, 1997] and the polar cap area [e.g., *Brinton et al.*, 1971; *Chandler et al.*, 1991; *Abe*
27 *et al.*, 1993; *Moore et al.*, 1997; *Su et al.*, 1998].

28 Above the open polar cap regions, where no hydrostatic equilibrium can be established,
29 low energy photoelectrons can escape the Earth's gravitational field. Consequently, a
30 spatial separation between the light electrons and the heavier ions (mainly H^+ , He^+ and
31 O^+) arises and an ambipolar electric field which eventually accelerates lighter ions upward
32 is set up. Once free of the gravitational potential, the polar wind expands at supersonic
33 speed along the magnetic field into the magnetotail lobes. This outflow of plasma from
34 the polar cap area is often referred to as the polar wind [*Banks and Holzer*, 1968; *Axford*,
35 1968; *Yau et al.*, 2007].

36 The ambient electric field associated with the polar wind is very small. Simulations
37 by *Su* [1998] suggest that the total potential drop of a few 10s of Volts extends over an
38 altitude of several Earth radii. Consequently, direct observations of this potential drop
39 is not possible, and only indirect methods can be used. *Kitamura et al.* [2012] used
40 the photoelectron flow data from the Fast Auroral SnapshoT (FAST) satellite during
41 geomagnetically quiet periods and inferred that potential drops above the satellite (ca

42 3800 km altitude) were typically around 20 V. Inferred potentials below the satellite were
43 much lower, only 1-3 V.

44 In a later follow-up study [*Kitamura et al.*, 2013], using data obtained during the main
45 and early recovery phases of geomagnetic storms, they reported typical potential drops of
46 5 V or less - i.e., much smaller than during quiet periods. They attributed this to stronger
47 convection of ions from the cusp area during disturbed conditions, which will effectively
48 reduce the effect of the photoelectrons.

49 Such low potential drops mean that little energy is available to accelerate ions in this
50 region. Additional acceleration, like e.g., centrifugal acceleration [e.g., *Cladis*, 1986; *Nils-*
51 *son et al.*, 2008, 2010] is not very effective over short distances [*Demars et al.*, 1996].
52 Unlike the cusp and cleft regions, there is no significant energization from solar wind
53 driven Poynting flux [e.g., *Zheng et al.*, 2005; *Strangeway et al.*, 2012] or wave activity
54 [e.g., *Wahlund et al.*, 1992; *Bouhram et al.*, 2004]. Thus, ions emanating from the polar
55 cap will not gain significant energy as they travel outwards - they will remain cold.

56 It is notoriously difficult to conduct in-situ measurements of the cold part of the out-
57 flowing ion population. In the tenuous plasma regions of the Earth's magnetosphere the
58 spacecraft voltage often reach several tens of volts positive due to photoelectron emissions
59 from the spacecraft surface. This spacecraft potential will prevent low energy ions from
60 reaching spacecraft sensors. Unless the effects of spacecraft charging can be eliminated,
61 cold ions therefore remain invisible for particle detectors.

62 Attempts to bypass this problem typically involve some form of active spacecraft po-
63 tential control. *Su et al.* [1998] used particle measurements from the Polar spacecraft
64 and presented a study of cold ion outflow during a limited time period when the onboard

65 Plasma Source Instrument (PSI) was operating and kept the spacecraft potential at a
66 few volts. They were then able to observe and characterize the polar wind outflow at
67 high altitudes for this time period. The Cluster spacecraft [*Escoubet et al.*, 1997] which
68 forms the observational basis for the present study, also has an Active Spacecraft Control
69 instrument [ASPOC - see *Riedler et al.*, 1997] but to our knowledge no specific study
70 focusing on polar wind or ion outflow has systematically utilized this.

71 *Engwall et al.* [2006] presented a completely different approach to cold ion outflow
72 detection. By utilizing data from two independent electric field instruments, they were
73 able to exploit the spacecraft charging and measurements from the two experiments to
74 derive densities and outflow velocities of cold plasma. This technique has also been applied
75 by a number of follow-up studies, e.g., *Engwall et al.* [2009a]; *Haaland et al.* [2012a, b];
76 *Li et al.* [2012, 2013]; *André et al.* [2015]; *Haaland et al.* [2015], and will also be applied
77 in the present study. The principles of this method will be described in section 2 of the
78 present paper.

79 The motivation for this paper was a call from the Geomagnetic Environment Modelling
80 (GEM) core group to provide observational inputs for benchmarking, parametrization and
81 verification of geophysical models valid during geomagnetic storms. During the years 2013
82 - 2015, the core group set up a project in which they selected three events to study closely:
83 an idealized synthetic event and two real geomagnetic storm events. Numerical modelers
84 were invited to simulate each and compare their results to other models. Additionally, data
85 experts and experimentalists were invited to share observations of the real-world events
86 and contribute to data-model comparisons. The present paper reports on observations of
87 cold ion outflow which may be useful for this purpose.

88 The paper is organized as follows: In section 2, we explain why cold ion measurement
89 are difficult and how the instrumentation onboard Cluster is used to bypass the spacecraft
90 charging problem. We also provide a description of the data set used for this study and
91 its characteristics. Section 3 presents the results, and section 4 discusses the implications.
92 Finally, section 5 summarizes the results.

2. The cold ion detection challenge

93 A spacecraft traversing the Earth's high altitude polar cap and magnetically connected
94 lobe region will be exposed to solar illumination. This illumination, in particular in the
95 extreme ultraviolet (UV) range, will cause photoionization of the spacecraft surface area.
96 In the tenuous plasma of the polar cap and lobes, the photoelectrons cannot easily be
97 replenished. Consequently, the spacecraft will be positively charged [see details in e.g.,
98 *Pedersen et al.*, 2001, 2008; *Lybekk et al.*, 2012]. Unless this charging can be prevented,
99 this will cause problems for low energy plasma measurements.

100 For Earth, escape energies for protons and Oxygen are around 0.6 and 10 eV, respec-
101 tively. Typically, there are no strong acceleration mechanisms above the polar cap region,
102 and a substantial amount of these cold outflowing ions will remain “cold” as they move
103 outwards. If the energy of these ions is below the spacecraft potential energy (eV_{SC} , where
104 e is elementary charge and V_{SC} is the spacecraft potential relative to the ambient plasma),
105 these ions will not be able to reach the detectors and are thus “invisible” as illustrated in
106 Figure 1.

107 Remote sensing of ion outflow is also difficult. Ground based measurements, e.g., inco-
108 herent scatter radars can only measure up to about 1000 km altitude. Vertical upward
109 motion, at these altitudes termed upwelling, often go along with downward vertical mo-

tion. It is thus difficult to assess how much plasma actually reaches escape velocity and actually escapes the Earth's gravitational field. Low orbit satellites, although less affected by spacecraft charging have similar issues.

2.1. Utilizing spacecraft potential and wake

The present study is based on observations from the Cluster constellation of spacecraft [Escoubet *et al.*, 1997]. A unique feature of the Cluster mission is the combination of two complementary electric field experiments, the Electric Field and Wave experiment [EFW - see Gustafsson *et al.*, 2001] and the Electron Drift Instrument [EDI - see Paschmann *et al.*, 1997; Quinn *et al.*, 2001] This combination is the key element for the technique to estimate cold ion flux developed by Engwall *et al.* [2006].

EFW is a classic double probe instrument, consisting of two pairs of boom mounted spherical probes. The probe to probe distance is approximately 88m for each pair. This arrangement provides measurements of the electric field in the satellite spin plane. Assuming no or negligible electric potential drop along the magnetic field ($E_{\perp} \gg E_{\parallel}$), the full 3D electric field can be estimated provided that the spin axis is not parallel to the magnetic field.

EDI is based on the drift of an electron gyro center in the presence of external forces. Each Cluster spacecraft is equipped with two EDI gun/detector units, each emitting a modulated electron beam with a fixed energy. (The beam energy can be switched between 500 eV and 1 keV to measure the effect of magnetic gradients, but as these are usually small compared to the local electron gyro radius, the beam energy is typically kept fixed at 1 keV). The firing direction of this beam is continuously controlled through a servo loop so that the coded beam returns to the detector unit. Gyro center position and

132 motion can then be determined from triangulation (or, in some regions, from the time-
 133 of-flight of the emitted electrons). For a known magnetic field with negligible gradients,
 134 the gyro center drift of the emitted beam is proportional to the convective electric field.
 135 In regions with fairly stable magnetic field, and low electron background plasma, EDI
 136 provides the full 3D convective electric field with very high accuracy. Strong variations
 137 in the magnetic fields or strong gradients can prevent successful tracking and no valid
 138 E-field can be calculated. Likewise, a strong electron background density can lead to an
 139 attenuation of the modulated beam, and tracking is lost.

140 Cluster consists of four identical spacecraft flying in a formation with variable separation
 141 distance. In the community, the spacecraft are simply referred to as C1, C2, C3 and
 142 C4. All four spacecraft are equipped with identical instruments, but EDI is only fully
 143 operational on C1 and C3.

144 2.1.1. Cold plasma density

145 With knowledge of surface properties and surface area and a known solar illumination,
 146 it is possible to use the spacecraft potential to estimate the ambient electron density, and
 147 thus the plasma density [e.g., *Pedersen et al.*, 2001; *Lybekk et al.*, 2012, and references
 148 therein]. In general, a relation of the form

$$N_e = Ae^{-BV_{SC}} + Ce^{-DV_{SC}} \quad (1)$$

149 exists, where N_e is the sought after electron density, V_{SC} is the spacecraft potential relative
 150 to the ambient plasma. The coefficients A,B,C and D are determined from calibrations
 151 against other measurements, and implicitly contain information about solar illumination
 152 and spacecraft surface properties.

153 2.1.2. Cold ion bulk velocity

154 If the bulk energy, E_K , of the cold ions flowing across the spacecraft is larger their
 155 thermal energy, kT_i , i.e., the following inequality exists

$$kT_i < E_K < eV_{SC}, \quad (2)$$

156 a wake void of ions will be formed downstream of the spacecraft. Electrons, however, with
 157 their higher mobility (typically $kT_e \gg E_{Ke}$), will be able to fill the wake. Consequently,
 158 an electric field, $E^{\vec{W}}$ along the bulk flow direction, \vec{u} will arise:

$$E^{\vec{W}} = g\vec{u} \quad (3)$$

159 where the scaling factor, g , is a function of the local plasma parameters, and can be
 160 experimentally determined [Engwall *et al.*, 2006].

161 The size of the wake is comparable to the boom-to-boom scale size of the spacecraft but
 162 much smaller than the gyro radius of the 1 keV electron beam emitted by EDI, which is
 163 of the order of several kilometers for the typical magnetic field strength in the lobes. The
 164 probe based measurements from EFW will thus be influenced by this artificial electric
 165 field whereas EDI is not affected. The wake electric field can then be expressed as a
 166 deviation between the wake influenced electric field measured by EFW, \vec{E}^{EFW} and the
 167 real, unperturbed ambient electric field \vec{E}^{EDI} :

$$E^{\vec{W}} = \vec{E}^{EFW} - \vec{E}^{EDI} = g\vec{u} \quad (4)$$

168 Note that the perpendicular part of the bulk flow, \vec{u}_\perp , is obtained directly from the EDI
 169 measurements $\vec{u}_\perp = \vec{E}^{EDI} \times \vec{B}/B^2$. The parallel component of u can then be obtained by
 170 decomposition \vec{E}^W into two spin plane component, E_x^W and E_y^W . An explicit expression
 171 for the parallel bulk velocity of the cold ions can then be obtained:

$$u_{||} = \frac{E_x^W u_{\perp, y} - E_y^W u_{\perp, x}}{E_y^W B_x - E_x^W B_y} \vec{B} \quad (5)$$

172 where B is the magnetic field.

173 Note that wake formation as such is not exclusive to the polar cap or lobe regions [e.g.,
 174 *Whipple et al.*, 1974, and references therein], but the combination of the two electric field
 175 measurements onboard Cluster has made determination of the bulk velocity possible for
 176 the first time.

177 2.1.3. Cold ion outflow flux

178 From the above equations 1 and 5, the flux of cold ions at the spacecraft position can
 179 now be determined:

$$f_{||} = N_e * u_{||} \quad (6)$$

180 Using flux conservation consideration and flux tube cross section from a magnetic field
 181 model, we can now scale this flux to ionospheric altitudes. Particle tracing can be used
 182 to determine the source region or fate of the outflowing ions [e.g., *Cully et al.*, 2003; *Li*
 183 *et al.*, 2012, 2013].

2.2. Limitations of the wake method

184 From the above derivation, one notes that it is not possible to distinguish between
185 different ion species. Nor is any distinction between different ion charge states possible,
186 so singly ionized ions are assumed in the above derivations. The wake method is more
187 sensitive to lighter ions, as these are more affected by the wake. Observations by *Su*
188 *et al.* [1998] indicate that Hydrogen is the dominant species in low-energy outflow from
189 the polar cap region. Nevertheless, in *Engwall et al.* [2009a] and *André et al.* [2015], the
190 derived densities have been lowered by a factor of 0.8 to account for the presence of heavy
191 ions. In reality, the abundance of heavier ions, typically Oxygen, in the outflow varies
192 both with geomagnetic activity and source location. Oxygen is more likely to emanate
193 from the cusp and auroral zone [e.g., *Yau and Andre, 1997; Lockwood et al., 1985b, a*].

194 The inequality in Equation (2), limits the temperature and bulk energy ranges of the
195 ions possible to detect. Also, since the velocity determination rests on the identification
196 and characterization of a downstream wake (which is not always observed - even in the
197 polar cap and lobe regions), the data set is not continuous in time, but consists of individ-
198 ual intermittent records. Furthermore, the bulk flow direction should have a significant
199 component along the spin plane of the spacecraft. Otherwise, the EFW probes will not be
200 able to measure the wake field. This is usually no issue in the lobes, where the magnetic
201 field is stretched out, but can be an issue closer to Earth.

202 As with any collection of experimental data, there are uncertainties related to measure-
203 ments, methodology and the underlying assumptions. *Engwall et al.* [2009a] estimated
204 that error due to methodology is of the order of $\pm 40\%$ or less for velocity calculations
205 and of the order of 20% for electron density calculations.

2.3. Source of cold ions

206 In order to calculate the total outflow of cold ions, we also need to know the area of the
207 source region, i.e., essentially the area of open magnetic flux in both hemispheres. In their
208 initial estimate of outflow rates, *Engwall et al.* [2009a] used a fixed polar cap boundary
209 located at 70° magnetic latitude. Neither expansion and contraction of the polar cap nor
210 any spatial inhomogeneities were taken into account. Later, *Haaland et al.* [2012a] used
211 a variable polar cap area, parametrized by the solar wind input energy after a method
212 developed by *Sotirelis et al.* [1998]. They noted large variations in the source area due to
213 the expansion and contraction of the polar cap in response to geoactivity.

214 *Li et al.* [2012] performed particle tracing to generate maps of the source area and could
215 thus also address any inhomogeneities in the source. Their results confirmed that the open
216 polar cap is the primary source of the cold ions, but they also found enhanced outflow
217 from a region near the cusp and a region near the nightside auroral zone during disturbed
218 conditions. Other than that, no significant day-night asymmetry in the outflow was
219 observed. Around equinox, most of the polar cap ionosphere is illuminated at least parts
220 of the day, both in northern and southern hemisphere, and this may explain the lack of a
221 pronounced dayside-nightside difference in outflow. Another factor is that convection and
222 vertical winds will cause some redistribution of the cold ions between the peak ionization
223 layers (the D,E and F layers of the ionosphere) and the topside ionosphere. There is
224 probably also mixing of ions from different ionospheric regions along the transport path
225 to the lobes where they are detected by Cluster.

226 Since the purpose of the present paper is to address the cold outflow during geomagnetic
227 storms, i.e., limited time periods, we use subsets of the full data set. The method of *Li*
228 *et al.* [2012] is therefore not applicable, since it requires full spatial coverage in order to

229 determine the size of the source area. We therefore use the procedure outlined in *Milan*
 230 [2009], which provide a proxy for the open flux area as function of dayside reconnection
 231 electric field, Φ_D and the Dst index (*Milan* [2009] actually uses the SYM-H index: see
 232 Section 2.4 for a discussion of various indices to characterize geomagnetic storms). The
 233 dayside reconnection field is a measure of opening of flux at the dayside magnetopause,
 234 and the Dst index provides a similar proxy for flux closure on the nightside. Any imbalance
 235 between these two processes will lead to an expansion or contraction of the area of open
 236 flux.

237 Based on 40'000 independent observations of auroral images, *Milan* [2009] came up with
 238 the following relation between Φ_D , Dst and the auroral oval radius:

$$\lambda = 18.2 - 0.038 Dst + 0.042 \Phi_D \quad (7)$$

239 where λ is the radius (in degrees) of the auroral oval. Note that the auroral oval, is not
 240 necessarily centered around any geomagnetic axis, so λ is in general not the co-latitude
 241 of the oval location. The dayside reconnection electric field is given by:

$$\Phi_D = 2.75 Re V_{SW} \sqrt{B_Y^2 + B_Z^2} \sin^2(\theta/2), \quad (8)$$

242 where $2.75 Re$ is a characteristic length scale, V_{SW} is the solar wind bulk flow speed, B_Y
 243 and B_Z are components of the interplanetary magnetic field, and θ is the IMF clock angle,
 244 here defined as $\theta = \arccos(B_Z / \sqrt{B_Y^2 + B_Z^2})$.

245 Expression (7) refers to the peak of the auroral oval as identified from the images. Our
 246 source area is poleward of the auroral oval. We have assumed an average auroral oval width

247 of approximately 5 degrees in latitude, and therefore shifted the open-closed boundary
 248 poleward by using a 2.5 degrees smaller radius for our source area. This poleward shift
 249 is consistent with open-closed-boundaries determined from in-situ particle measurements
 250 [see e.g., discussion in *Boakes et al.*, 2008, and references therein.]

251 At 1000 km altitude, one degree in latitude corresponds to approximately 128 km. The
 252 size of the source area in one hemisphere, A , can thus be expressed as:

$$\begin{aligned}
 A &= \pi [\lambda * 128 \text{ km}]^2 \\
 &= \pi [(15.7 - 0.038 \text{ Dst} + 0.042 \Phi_D) * 128 \text{ km}]^2
 \end{aligned}
 \tag{9}$$

253 All of the above used quantities are known and available from our data set, and we can
 254 thus calculate the total area (both hemispheres) of the source of cold ions for a given
 255 combination of disturbance level and solar wind input.

2.4. Data set Overview

256 In the present study, we combine several data sets, already described in previous pub-
 257 lications:

258 First, we use an extended set of wake observations which provides parallel bulk flow
 259 velocities of the cold ions. This extended data set contains observations from Cluster
 260 C1 and C3. The data set was prepared and presented by *André et al.* [2015], and is
 261 based on an earlier, similar data set prepared by [*Engwall et al.*, 2009a]. The new wake
 262 data set contains about twice as many observations as the earlier set of observations
 263 (approximately 350'000 records in *André et al.* [2015] versus 176'000 records in *Engwall*
 264 *et al.* [2009a]). In addition to the full processing for Cluster spacecraft 1, the new data set

265 contains 5 more years of observations, and thus cover almost a full solar cycle (2001-2010).
266 Since the data set relies on the detection and characterization of an electrostatic wake,
267 observations are only available intermittently, and only when Cluster traverses the high
268 latitude nightside lobes, i.e., in the period July to November each year. Several studies
269 have utilized these wake data sets, e.g., *Engwall et al.* [2009b]; *Nilsson et al.* [2010, 2012];
270 *Haaland et al.* [2012a, b]; *Haaland et al.* [2015]; *Li et al.* [2012, 2013].

271 Cold ion densities are based on measurements reported by *Lybekk et al.* [2012]. This
272 data set contains data from all four Cluster spacecraft for the period 2001-2010. In the
273 present study, we only use data from Cluster C1 and C3 since these are the only spacecraft
274 with usable wake observations. Convection measurements, used to study the transport
275 of plasma, are discussed in *Haaland et al.* [2008, 2009], and based on EDI measurements
276 from Cluster C1 and C3 for 2001-2010.

277 In addition to the above, we also use auxiliary parameters such as solar wind data,
278 geomagnetic indices and the F10.7 index - a daily proxy for solar UV illumination.

279 To characterize the geomagnetic disturbance level, we use SuperMag-based partial ring
280 current indices [SMR - see *Gjerloev*, 2012; *Newell and Gjerloev*, 2012]. The standard SMR
281 index is essentially the same as the Disturbed Storm Time index [Dst - see *Sugiura*, 1964]
282 or the similar SYM-H index [*Wanliss and Showalter*, 2006] but is constructed from a larger
283 number of observatories. SYM-H and SMR are available at one-minute time resolution,
284 whereas the original Dst index is a hourly average. All three indices are measurements of
285 perturbations in the horizontal component of the Earth's magnetic field around equatorial
286 latitudes, and provide a proxy for the energy in the Earth's ring current.

287 Density and convection measurements are available at almost all times when Cluster is
288 in the lobes or polar cap regions. However, a full characteristics of the cold ion outflow
289 is only possible when both wake observations and convection measurements are present.
290 Figure 2 shows the SMR index for 2001-2010, with periods where wake measurements
291 could be utilized indicated in red.

292 The wake dataset is somewhat biased towards moderately disturbed conditions. On
293 one hand, utilization of the wake requires a certain bulk velocity (see Equation 2) and
294 minimum solar illumination (see section 2.1). This situation is more likely during slightly
295 disturbed conditions and thus negative SMR values. On the other hand, very disturbed
296 conditions with rapidly changing magnetic field will cause the EDI instrument to lose
297 tracking. Consequently, the outflow velocity (Equation 5) cannot be determined. Another
298 reason for less contribution from very disturbed conditions may be that the ions are more
299 often heated to energies above our detection limit. The overall average SMR value in our
300 data set is approximately -20 nT and the average F10.7 index is 137. The most intense
301 storm during the years 2001-2010, in terms of SMR deflection, took place in October 2003,
302 when the SMR index dropped below -500 nT. There are no wake observations during this
303 minimum, so the minimum SMR value in our data set is -409 nT, also observed in October
304 2003.

3. Observations of cold ion outflow during geomagnetic storms

305 Geomagnetic storms are large scale global disturbances in the Earth's magnetic field,
306 typically lasting a couple of days. The time evolution of storms is characterized in terms
307 of three phases referred to as the initial, main and recovery phase, respectively. These
308 stages of storm evolution can be identified from the behavior of the SMR (Dst) index as

309 illustrated in Figure 3a). For comparison, panels b) and c) show the SMR index for the
310 two storms selected by the GEM community for benchmarking and comparison. These
311 will be discussed in some detail in the following subsections.

312 The initial phase, sometimes referred to as a storm sudden commencement (SSC), is
313 characterized by a positive perturbation in Dst, and mainly caused by a compression of
314 the geomagnetic field, often in connection with the arrival of a coronal mass ejection.
315 The compression of the magnetosphere will also cause an increase in the density of the
316 lobes [e.g. *Svenes et al.*, 2008; *Lybekk et al.*, 2012]. Since the cold ion flux is a product
317 of velocity and density (see Equation 6), there will be an apparent increase in outflow
318 during this compression. It is important to note that this apparent increase is primarily a
319 compressional effect, and not necessarily caused by additional supply from the ionosphere.

320 The main phase, marked with red color in Figure 3a), is characterized by a significant
321 drop in the SMR index over a period of typically 2-10 hours. The main phase is a
322 consequence of enhanced transport of plasma inside the magnetosphere and a buildup of
323 energy in the ring current.

324 During the recovery phase, marked green in Figure 3a) various loss processes will lead
325 to a reduction in the ring current, and SMR returns to non-storm values. Loss processes
326 are slower than the main phase buildup, and a recovery phase can last for several days.

327 In addition, we introduce an additional stage, labelled ③, which we shall refer to as
328 the “peak phase”, which overlaps with the late main and early recovery phase. The peak
329 phase describes the interval where the SMR index exceeds 75% of its peak value.

3.1. The GEM storm on 30 Sep - 5 Oct 2002

330 The GEM core group selected two real-world events for model benchmarking and com-
331 parisons between models and observations. The first event selected was a storm period
332 starting around 1 October 2002. The left panels of Figure 4 give an overview of observa-
333 tions and some derived quantities during this storm.

334 As guidelines, horizontal blue dashed lines and values in panels f) to i) indicate average
335 (median) quiet time values for density, velocities and flux. Note that the flux is mapped
336 to ionospheric altitudes (1000km) so scaling due to flux tube expansion with increasing
337 altitude has been taken into account, but average density and average velocities are based
338 on local measurements at a range of Cluster altitudes.

339 Wake observations and thus the ability to fully characterize the cold ion outflow during
340 this storm are limited, possibly due to strong heating and thus ion energies above our
341 detection limit. Panel a) of Figure 4 shows the XZ_{GSE} projection of the Cluster C3 orbit
342 (dashed line; Cluster C1 is close nearby) with coverage for C1 indicated as thick black
343 line segments and the coverage C3 as thick green line segments.

344 The IMF is strongly northward for several hours prior to the storm, and despite a sharp
345 jump in the solar wind dynamic pressure (panel e), the 1-5 October 2002 storm lacks a
346 clear initial phase. As the IMF turns southward around 04 UT on 1 Oct, a rather large and
347 fast drop (about 180 nT within 8 hours) in the SMR index, indicating a fast energization of
348 the ring current, is observed. There is only a gradual increase in the solar wind dynamic
349 pressure (panel e) during the main phase, so the storm is primarily driven by strong
350 dayside reconnection following the southward directed IMF. Consequently, an imbalance
351 between dayside reconnection (opening of flux) and nightside reconnection (closing of flux)

352 arises, and the polar cap area, shown in panel c), increases rapidly to almost 3 times its
353 pre-storm area.

354 SMR reaches its peak value of -181 nT around noon on 1 October 2002. A second,
355 less pronounced drop in SMR is observed around 03 UT on 2 October followed by minor
356 fluctuations in SMR. The recovery phase is also interrupted by a new intensification
357 starting on 3 October.

358 Wake observations are available from two intervals. First, a few hours of observations
359 starting early on 2 October, some hours after the SMR minimum of the storm, but still
360 within the stage we have termed “peak phase”. Cluster is then traversing tailward in
361 the northern lobe. No further wake observations are available until Cluster returns to
362 this region after one orbit (orbit period ≈ 57 hours) on 4 October, corresponding to the
363 recovery of the second intensification. One could argue that the new activation on 3
364 October should be classified as a new storm. Still, in the text below, we discuss this event
365 as one storm event, and refer to the two intervals with observations as the peak phase
366 and the recovery phase of a single storm.

367 The daily F10.7 index, shown as a histogram in panel d), increases from 136 mWm^2
368 on 2 October to 155 mWm^2 on 4 October 2002. Periods with wake observations are
369 indicated in black and thicker lines. Recall that an increase in F10.7 indicates additional
370 solar irradiance and thus potentially more ionization and consequently enhanced cold ion
371 outflow [e.g., *André et al.*, 2015].

372 Some care must be taken when interpreting the measured density, shown in panel f).
373 Although the highest densities are observed early on 2 October, one should have in mind
374 that these observations are taken closer to Earth (radial distances 6 - 7 Re) than the later

375 observations on 4 October (radial distances 7 - 16 Re). The solar wind dynamic pressure
376 is also higher during the first period of observations, and parts of the apparent enhanced
377 density may be due to a compression of the whole magnetosphere as discussed in Section
378 3.

379 Panel g) shows outward parallel bulk velocity of the cold ions. Earlier studies using the
380 cold ion data set have shown that the outward parallel velocity increases with geocentric
381 distance [see e.g., Figure 6 in *Engwall et al.*, 2009a]. Indeed, mean and median outflow
382 velocities are lower during the peak phase on 2 Oct than during the recovery phase on
383 4 Oct. This may be related to the findings by *Kitamura et al.* [2013] who found a lower
384 ambient electric field (and thus less acceleration) during main and early recovery phases
385 (which corresponds to our peak phase) than during quiet times. However, there are large
386 variabilities, with velocities ranging from 10-80 km/s for the peak phase and from 5 to
387 more than 100 km/s during the recovery phase.

388 Panel h) shows the mapped flux, i.e., flux at ionospheric altitudes (1000km) where
389 scaling due to flux tube expansion with increasing altitude has been taken into account.
390 This panel clearly indicates a higher ionospheric outflow flux during the most disturbed
391 period around 2 October than the later observations in the recovery phase on 4 October.
392 Finally, panel i) shows one-minute averages of convection. The convection is essentially
393 in the Z_{GSM} direction, i.e., towards the plasma sheet.

394 Table 1 summarizes the observations. We have here calculated median values over the
395 two stages of the storm where there are observations. The columns are labelled A to I for
396 easy referencing and navigation.

397 The first period of observation contains a total of 575 records of wake observations, and
398 are available during a 3 hour period between around 01 UT to 04 UT on 2 October (note
399 that the given time intervals in column C indicate where some data was available, but do
400 not necessarily contain continuous, uninterrupted measurement series, and not necessarily
401 the full time span of the storm phase). The median SMR value for this collection is -149
402 nT, and this period thus correspond to the late part of the peak phase, of the storm.
403 This period is characterized by a significantly higher (than non-storm times) flux and an
404 expanded polar cap region. Consequently, the total outflow rate, $2.22 \cdot 10^{26} s^{-1}$, is also
405 significantly higher than quiet time values (see below) and also significantly higher than
406 values of H⁺ and O⁺ outflow reported for disturbed periods in earlier studies [e.g., *Yau*
407 *et al.*, 1985a].

408 The second period with wake observations, in total 2310 records over the 10 hour period
409 from 10:10 to 22:10 UT on 4 October is still characterized by a large negative SMR value
410 (median SMR is -95 nT). Both mapped flux and total polar area have decreased since the
411 peak phase, and the resulting outflow is consequently smaller than during the peak phase.

3.2. The GEM storm on 23 - 28 Oct 2002

412 The second storm selected by the GEM community for benchmarking is the result of a
413 corotating interaction region, and commences around 15:00 UT on 23 October, with the
414 main phase starting early 24 October 2002. Details are shown in the right row of panels
415 in Figure 4.

416 Being almost a solar rotation after the first event, the Cluster orbit has precessed about
417 2 hours in local time towards dusk.

418 This storm is weaker, with a minimum SMR of around -97 nT (panel b). The main
419 phase is longer than for the first event and also shows signatures of individual substorms.
420 There is about 30 hours between the SSC on 23 October and the minimum SMR around
421 20:30 UT on 24 October.

422 The variation in source area (panel c) is also much smaller in this case. From an initial
423 size of just above 10^7 km² prior to the storm, the total polar cap area expands to about
424 $4 \cdot 10^7$ km² around the peak phase on 24 October.

425 The solar wind dynamic pressure shows a very similar behavior as the previous event,
426 with an initial pressure pulse and a gradual increase during the first half of the main
427 phase. F10.7, and thus ionization, is highest during the peak phase of the storm (though
428 there is probably no direct causal relation between the F10.7 index and storm phase).

429 Observations of cold ion outflow, shown in panels g) and h), are available from around
430 10:27 UT on 23 Oct when Cluster was in the southern hemisphere until around 23:55 UT
431 on 25 October. All measurements were taken between 6 and 19 Re geocentric distance,
432 and unlike the previous events, we have observations from all phases of the storm for this
433 event. As for the previous event, there is significant spread in the measurements. Perhaps
434 the most pronounced feature in the observations is the distinctly higher flux (panel h))
435 during the peak phase.

436 We also note that the plasma convection (panel i)) picks up rapidly as the main phase
437 of the storm progresses, and subsides as the storm abates.

438 Table 2 lists averages for this storm. Despite similar solar wind dynamic pressure
439 values, average cold ion densities are consistently lower than for event 1. With exception

440 of the main phase, from which there are only 128 records with wake observations, outflow
441 velocities are fairly constant and in the same range as for event 1.

3.3. A generic geomagnetic storm

442 A typical geomagnetic storm lasts a couple of days. Wake characterisation, and thus
443 cold ion outflow measurements are only available for at best a few hours when the Cluster
444 satellites traverses the lobes, and often only intermittently. The two selected GEM events
445 above are examples of this. Thus, we do not have full coverage of cold ion observations
446 throughout any of the storms in Figure 2. Still, we can combine observations from several
447 storms to gain knowledge about cold ion outflow during storms in general.

448 During the years 2001-2010, we visually identified a total 32 geomagnetic storms where
449 cold ion data was available for at least some intervals in both the main and recovery
450 phase. For each of these storms, we recorded start times and durations of the various
451 storm phases and added this information to the cold ion database. The peak (minimum)
452 value of the SMR index for each storm was also noted.

453 For better parametrization, we made a further division of the storm evolution. In the
454 left panel of Figure 3 we have labelled these stages with numbers ① to ④. Not all storms
455 exhibit a pronounced initial phase (labelled ①), so we will not focus much on this stage.

456 First, we divide the main phase into an early and a late stage (labelled ②a, ②b), where
457 the early stage contains the first half of the SMR drop until minimum, and the second
458 stage is the time until the peak SMR is reached.

459 We do a similar division of the recovery phase. The label ③a refers to the early recovery
460 and the label ③b refers to the late recovery stage. The classification of this latter stage
461 is subject to some uncertainty, as it is not always easy to accurately determine when

462 the effects of a storm have fully subsided. There are also intervals where a new storm
463 commences in what appears to be the late recovery of an earlier storm.

464 As noted above we have introduced an additional stage (the “peak phase”) labelled ③,
465 which describes the interval where the SMR index exceeds 75% of its peak value. The
466 peak phase consists of the late main and early recovery phase.

467 Our generic storm is simply constructed by the taking the averages (medians) of the
468 various parameters over these 32 storms. Table 3 summarizes the data characteristics of
469 our generic storm. For comparison, we also include quiet time periods, where “quiet”
470 is simply defined as all intervals where the SMR index is positive, and no storms were
471 identified.

472 We also investigated whether there are any fundamental differences in ion outflow be-
473 tween weak and strong storms (several SMR ranges were tested to define “weak” and
474 “strong”). Densities, outflow velocities and fluxes were lower for weak storms, but the
475 general behaviour of increasing outflow as the main phase progresses, strongest outflow
476 during the peak phase and a gradual abatement during the recovery phase did not change.

4. Discussion

477 Figure 4 together with tables 1, 2 and 3 draw a fairly consistent picture of cold ion
478 outflow during geomagnetic storms: Cold ion outflow increases with increasing storm
479 intensity, and the largest outflow is observed around the peak phase of a storm. During
480 the recovery phase, the outflow subsides, but is still stronger than during quiet times.
481 Below, we discuss the observations, in particular those listed in Table 3, in some detail,
482 and try to identify processes responsible for the observed behaviour.

4.1. Variations in density and velocity during storms

483 The observations above indicate that the density (column E in Tables 1, 2 and 3)
484 increases throughout the main phase, reaches a maximum when the storm reaches its late
485 main phase or peak phase and decreases as the effects of the storm subside during the
486 recovery phase.

487 As mentioned above, some caution is required when interpreting density values. In
488 addition to the altitude of the observations, variations in the observed density can be due
489 to several processes, of which the most probable are: 1) a genuine increase in the supply
490 of plasma from the ionosphere; 2) compression of the whole magnetosphere; 3) “con-
491 tamination” through inflow of magnetosheath plasma following dayside or high-latitude
492 reconnection.

493 Ideally, our measurements should only be sensitive to the first process, but there is no
494 way to actually identify the relative contributions of the above processes. Magnetosheath
495 plasma typically has higher temperatures, but recall that the cold plasma density is derived
496 from the spacecraft voltage, and even magnetosheath-like plasma can affect the spacecraft
497 voltage. “Contamination” from other sources can therefore not be excluded [e.g., *Pedersen*
498 *et al.*, 2001].

499 There is only a weak correlation between the solar wind dynamic pressure and the
500 observed density (linear Pearson correlation coefficient = 0.26) so compression of the
501 magnetosphere alone cannot explain the observed variations in cold ion density throughout
502 storms seen in Table 3.

503 Increased Joule heating in the ionosphere [e.g., *Rodger et al.*, 2001] and other heating
504 processes raise the scale height of both neutral and ionized components of the thermo-

505 sphere, resulting in increased ion density above the exobase and thus increase the source
506 reservoir. This may explain some of the observed density variations throughout storms.
507 During very disturbed conditions a larger fraction of the ions will probably be heated to
508 energies above our detection limit (≈ 70 eV), though.

509 Variations in bulk outflow velocity (column F) are smaller than the density variations.
510 Table 3 shows that the bulk velocity is highest during the peak phase of the storm. Parallel
511 bulk flow velocities are derived from wake observations, and thus only sensitive to cold
512 ions (see Section 2.1.2). They are thus less ambiguous than density values. We note that
513 the maximum velocities in Tables 1 and 2 seem to be in the recovery and main phase,
514 respectively. The limited data coverage may be one possible reason for this apparent
515 discrepancy.

516 At low altitudes, acceleration is primarily caused by an imbalance between the down-
517 ward gravity and upward forces from the ambient electric fields and the mirror force.
518 Probably, neither of these forces vary greatly throughout storm phases, however. From
519 the results of *Kitamura et al.* [2013], one would even expect the ambient electric field in
520 the polar cap region to be smaller during disturbed periods. During periods with high
521 geomagnetic activity, additional parallel fields may play a role near the cusp and auroral
522 zone, but less so in the open polar cap area.

523 At Cluster altitudes, centrifugal acceleration, although small, is the only relevant force.
524 Centrifugal acceleration is governed by magnetospheric convection which is higher during
525 disturbed periods. We thus argue that the observed variations in velocity throughout the
526 storm phases are a result of field aligned acceleration caused by centrifugal forces working

527 over long distances. This is corroborated by the fact that the parallel velocity is more or
528 less proportional to the convection in the tables.

529 Note that the low cold ion outflow velocities imply long transport times (typically of
530 the order of hours) from the ionosphere to the lobes where our observations are made.
531 Although these transport times are smaller than typical timescales of the various storm
532 phases, it might nonetheless be important for modelers.

4.2. Variations in source area and flux of cold ions

533 The mapped flux (column G) is a product of the locally measured density and bulk
534 velocity, but mapped to ionospheric heights (1000 km). The mapped flux show strong
535 variations as the storm progresses, with the maximum flux, $5.31 \cdot 10^8 \text{ cm}^{-2} \text{ s}^{-1}$, at the peak
536 phase of the storm. This value is more than 3 times higher than the quiet time flux. As
537 the storm subsides, the flux decreases.

538 The source area given in column H in Tables 1, 2 and 3 are calculated using the assump-
539 tion that the open polar cap is the source of the cold ions. We see the same trend in the
540 polar cap area as the other parameters; the source area increases in size as the intensity
541 of the storm increases and reaches a maximum when the storm is at its most intense and
542 decreases as the storm subsides.

543 Models [e.g., *Cully et al.*, 2003; *Ebihara et al.*, 2006] and observations [e.g. *Moore et al.*,
544 1999; *Haaland et al.*, 2012a; *Li et al.*, 2013] have shown that the fate of outflowing ions
545 is largely governed by the convection. High convection means a faster transport to the
546 plasma sheet and essentially no ion escape direct into the solar wind along open field lines.

547 The observations summarized in Tables 1, 2 and 3 are taken at a range of altitudes. Due
548 to the evolution of Cluster's orbit, with the line of apsides moving down as time progresses,

549 there are more observations from southern hemisphere. Southern hemisphere observations
550 are on average taken at higher altitudes than northern hemisphere observations.

551 Since we scale flux values to ionospheric altitudes, the actual fluxes are not affected, but
552 there will be an orbital bias: Consider the situation illustrated schematically in Figure
553 5. During quiet periods with low or stagnant convection, the effective transport path for
554 cold ions from a given dayside source will be along the blue arrow. This outflow will be
555 detected by a spacecraft located in the vicinity of region B, i.e., rather high altitudes and
556 over an extended time period.

557 During disturbed condition, the convection is stronger, and the effective transport path
558 will be along the orange arrow and can only be detected when Cluster is around region
559 A, i.e., at lower altitudes and for shorter time periods.

560 This bias is also present in our characteristic data set in Table 3. Main phase and peak
561 phase measurements are on average taken at lower altitudes than during quiet times and
562 recovery time observations.

4.3. Accumulated outflow during a storm

563 Table 3 also allows us to estimate the total cold ion outflow throughout a storm. Our
564 generic storm has a duration of almost 100 hours (column C in Table 3, but taking into
565 account that the “peak phase” overlaps with the main and recovery phases). If we take
566 the durations of the individual phases, and multiply with the respective average outflow
567 rates (column I) we obtain a total outflow of approximately $7 \cdot 10^{32}$ ions. For comparison,
568 the non-storm total outflow over the same time period would be of the order $3.5 \cdot 10^{32}$
569 ions.

570 Since storm times are associated with enhanced convection (column J), the outflow
571 is more likely to be transported to the plasma sheet [*Haaland et al.*, 2012a; *Li et al.*,
572 2013], whereas during stagnant convection, a larger fraction of the outflowing ions are
573 lost downtail into the solar wind. The technique used in present study is not able to
574 resolve composition, but earlier results [see e.g., *Kistler et al.*, 2006, and references therein]
575 indicate that the O⁺ abundance and thus the O⁺/H⁺ ratio increase significantly during
576 storm times. In terms of mass transport, the supply to the near Earth plasma sheet is
577 therefore much larger than the factor 2 change in cold ion outflow between quiet time and
578 storm time.

5. Summary

579 We have presented observations of cold ion outflow during two selected geomagnetic
580 storm events, and calculated characteristic outflow parameters which may be useful for
581 benchmarking against models and simulations. The observational results can be summa-
582 rized as follows:

- 583 • At a given location, cold ion density in the lobe region varies with storm intensity.
584 Higher geomagnetic activity (characterized by larger negative SMR values) is associated
585 with higher cold ion densities. Average lobe densities at Cluster altitudes (4 - 19 Re) vary
586 between 0.13 cm^{-3} during quiet times to about 0.4 cm^{-3} during disturbed periods.
- 587 • Variations in bulk outflow velocity also show correlation with storm intensity, al-
588 though the variations are typically 50 % or less between the lowest outflow velocities
589 observed during quiet times and the highest outflow velocities observed during the peak
590 intensity of the storm. The increased bulk outflow velocity is probably a result of larger
591 centrifugal forces due to enhanced convection during disturbed conditions.

- 592 • The flux of cold ions from the ionosphere is of the order of $1 \cdot 10^8 \text{ cm}^{-2} \text{ s}^{-1}$ during
593 quiet times and more than 5 times higher during storm maximum.
- 594 • The source area, assumed to be the open polar cap regions, vary significantly with
595 storm intensity. During the peak phase of the storm, the source area is typically almost
596 twice as large as the quiet time area.
- 597 • Outflow rates vary almost an order of magnitude between quiet and very disturbed
598 condition. The average quiet time outflow was $0.3 \cdot 10^{26} \text{ s}^{-1}$, increasing to a maximum of
599 $2.7 \cdot 10^{26} \text{ s}^{-1}$, during the peak phase of our characteristic storm.
- 600 • During a typical storm (i.e., our 'generic storm'), the total accumulated outflow is of
601 the order $7 \cdot 10^{32}$ ions, which is roughly twice as much as during quiet time conditions.
- 602 • During disturbed periods, convection is stronger, and the outflowing cold ions are
603 more likely to be supplied to the near-Earth plasma tail.

Appendix: Storm list

604 Table 4 lists the dates and times of geomagnetic storm periods used to estimate char-
605 acteristic cold ion outflow key parameters during geomagnetic storms. Note that this list
606 only shows intervals of storms where we have some observations during the main and
607 recovery phase. In general we do not have full coverage during a storm. Cold ion data
608 are only available during late July to early November when Cluster has its apogee in the
609 geomagnetic tail.

610 **Acknowledgments.** This study was supported by the Norwegian Academy of Science
611 and Letters and the Fritjof Nansen Fund for Scientific Research. We also thank the staff
612 at EISCAT Svalbard for their support during field work in Svalbard. Computer code used

613 for the calculations in this paper has been made available as part of the QSAS science
614 analysis system. Solar wind data were obtained from the Coordinated Data Analysis
615 Web (CDAWeb - see <http://cdaweb.gsfc.nasa.gov/about.html>). We also thank the Inter-
616 national Space Science Institute, Bern, Switzerland for providing computer resources and
617 infrastructure for data exchange.

References

- 618 Abe, T., B. A. Whalen, A. W. Yau, R. E. Horita, S. Watanabe, and E. Sagawa, EXOS D
619 (Akebono) suprathermal mass spectrometer observations of the polar wind, *J. Geophys.*
620 *Res.*, , *98*, 11,191, 1993.
- 621 André, M., and C. M. Cully, Low-energy ions: A previously hidden solar system particle
622 population, *Geophys. Res. Lett.*, , *39*, 3101, 2012.
- 623 André, M., P. Norqvist, L. Andersson, L. Eliasson, A. I. Eriksson, L. Blomberg, R. E.
624 Erlandson, and J. Waldemark, Ion energization mechanisms at 1700 km in the auroral
625 region, *J. Geophys. Res.*, , *103*, 4199–4222, 1998.
- 626 André, M., K. Li, and A. I. Eriksson, Outflow of low-energy ions and the solar cycle, *J.*
627 *Geophys. Res.*, , *120*, 1072–1085, 2015.
- 628 Axford, W. I., The polar wind and the terrestrial helium budget, *J. Geophys. Res.*, , *73*,
629 6855–6859, 1968.
- 630 Banks, P. M., and T. E. Holzer, The polar wind, *J. Geophys. Res.*, , *73*, 6846–6854, 1968.
- 631 Boakes, P. D., S. E. Milan, G. A. Abel, M. P. Freeman, G. Chisham, B. Hubert, and
632 T. Sotirelis, On the use of IMAGE FUV for estimating the latitude of the open/closed
633 magnetic field line boundary in the ionosphere, *Annales Geophysicae*, *26*, 2759–2769,

- 634 2008.
- 635 Bouhram, M., B. Klecker, W. Miyake, H. Rème, J. Sauvaud, M. Malingre, L. Kistler, and
636 A. Blagau, On the altitude dependence of transversely heated O distributions in the
637 cusp/cleft, *Annales Geophysicae*, *22*, 1787–1798, 2004.
- 638 Brinton, H. C., J. M. Grebowsky, and H. G. Mayr, Altitude variation of ion composition
639 in the midlatitude trough region: Evidence for upward plasma flow, *J. Geophys. Res.*,
640 , *76*, 3738–3745, 1971.
- 641 Chandler, M. O., T. E. Moore, and J. H. Waite, Jr., Observations of polar ion outflows,
642 *J. Geophys. Res.*, , *96*, 1421–1428, 1991.
- 643 Chappell, C. R., T. E. Moore, and J. H. Waite, Jr., The ionosphere as a fully adequate
644 source of plasma for the earth's magnetosphere, *J. Geophys. Res.*, , *92*, 5896–5910,
645 1987.
- 646 Chappell, C. R., B. L. Giles, T. E. Moore, D. C. Delcourt, P. D. Craven, and M. O.
647 Chandler, The adequacy of the ionospheric source in supplying magnetospheric plasma,
648 *Journal of Atmospheric and Solar-Terrestrial Physics*, *62*, 421–436, 2000.
- 649 Cladis, J. B., Parallel acceleration and transport of ions from polar ionosphere to plasma
650 sheet, *Geophys. Res. Lett.*, , *13*, 893–896, 1986.
- 651 Cully, C. M., E. F. Donovan, A. W. Yau, and G. G. Arkos, Akebono/Suprathermal Mass
652 Spectrometer observations of low-energy ion outflow: Dependence on magnetic activity
653 and solar wind conditions, *J. Geophys. Res.*, , *108*, 1093, 2003.
- 654 Demars, H. G., A. R. Barakat, and R. W. Schunk, Effect of centrifugal acceleration on
655 the polar wind, *J. Geophys. Res.*, , *101*, 24,565–24,572, 1996.

- 656 Ebihara, Y., M. Yamada, S. Watanabe, and M. Ejiri, Fate of outflowing suprathermal
657 oxygen ions that originate in the polar ionosphere, *J. Geophys. Res.*, , *111*, 4219, 2006.
- 658 Engwall, E., A. I. Eriksson, M. André, I. Dandouras, G. Paschmann, J. Quinn, and
659 K. Torkar, Low-energy (order 10 eV) ion flow in the magnetotail lobes inferred from
660 spacecraft wake observations, *Geophys. Res. Lett.*, , *33*, 6110, 2006.
- 661 Engwall, E., A. I. Eriksson, C. M. Cully, M. André, P. A. Puhl-Quinn, H. Vaith, and
662 R. Torbert, Survey of cold ionospheric outflows in the magnetotail, *Annales Geophysicae*,
663 *27*, 3185–3201, 2009a.
- 664 Engwall, E., A. I. Eriksson, C. M. Cully, M. André, R. Torbert, and H. Vaith, Earth's
665 ionospheric outflow dominated by hidden cold plasma, *Nature Geoscience*, *2*, 24–27,
666 2009b.
- 667 Escoubet, C. P., R. Schmidt, and M. L. Goldstein, Cluster - Science and Mission Overview,
668 *Space Sci. Review*, *79*, 11–32, 1997.
- 669 Gjerloev, J. W., The SuperMAG data processing technique, *J. Geophys. Res.*, , *117*, 9213,
670 2012.
- 671 Gustafsson, G., M. André, T. Carozzi, A. I. Eriksson, C.-G. Fälthammar, R. Grard,
672 G. Holmgren, J. A. Holtet, N. Ivchenko, T. Karlsson, Y. Khotyaintsev, S. Klimov,
673 H. Laakso, P.-A. Lindqvist, B. Lybekk, G. Marklund, F. Mozer, K. Mursula, A. Ped-
674 ersen, B. Popielawska, S. Savin, K. Stasiewicz, P. Tanskanen, A. Vaivads, and J.-E.
675 Wahlund, First results of electric field and density observations by Cluster EFW based
676 on initial months of operation, *Annales Geophysicae*, *19*, 1219–1240, 2001.
- 677 Haaland, S., G. Paschmann, M. Förster, J. Quinn, R. Torbert, H. Vaith, P. Puhl-Quinn,
678 and C. Kletzing, Plasma convection in the magnetotail lobes: statistical results from

- 679 Cluster EDI measurements, *Annales Geophysicae*, *26*, 2371–2382, 2008.
- 680 Haaland, S., B. Lybekk, K. Svenes, A. Pedersen, M. Förster, H. Vaith, and R. Torbert,
681 Plasma transport in the magnetotail lobes, *Annales Geophysicae*, *27*, 3577–3590, 2009.
- 682 Haaland, S., A. Eriksson, E. Engwall, B. Lybekk, H. Nilsson, A. Pedersen, K. Svenes,
683 M. André, M. Förster, K. Li, C. Johnsen, and N. Østgaard, Estimating the capture and
684 loss of cold plasma from ionospheric outflow, *J. Geophys. Res.*, , *117*, 7311, 2012a.
- 685 Haaland, S., K. Svenes, B. Lybekk, and A. Pedersen, A survey of the polar cap density
686 based on Cluster EFW probe measurements: Solar wind and solar irradiation depen-
687 dence, *J. Geophys. Res.*, , *117*, 1216, 2012b.
- 688 Haaland, S., M. André, A. Eriksson, K. Li, H. Nilsson, L. Baddeley, C. Johnsen, L. Maes,
689 B. Lybekk, and A. Pedersen, *Magnetosphere-Ionosphere Coupling in the Solar System*,
690 Chap. 1, AGU/Wiley, 2015 (in review).
- 691 Horwitz, J. L., The ionosphere as a source for magnetospheric ions, *Reviews of Geophysics*
692 *and Space Physics*, *20*, 929–952, 1982.
- 693 Kistler, L. M., C. G. Mouikis, X. Cao, H. Frey, B. Klecker, I. Dandouras, A. Korth,
694 M. F. Marcucci, R. Lundin, M. McCarthy, R. Friedel, and E. Lucek, Ion composition
695 and pressure changes in storm time and nonstorm substorms in the vicinity of the
696 near-Earth neutral line, *J. Geophys. Res.*, , *111*, 11,222, 2006.
- 697 Kitamura, N., K. Seki, Y. Nishimura, N. Terada, T. Ono, T. Hori, and R. J. Strangeway,
698 Photoelectron flows in the polar wind during geomagnetically quiet periods, *J. Geophys.*
699 *Res.*, , *117*, 7214, 2012.
- 700 Kitamura, N., K. Seki, Y. Nishimura, T. Hori, N. Terada, T. Ono, and R. J. Strangeway,
701 Reduction of the field-aligned potential drop in the polar cap during large geomagnetic

- 702 storms, *J. Geophys. Res.*, , 118, 4864–4874, 2013.
- 703 Li, K., S. Haaland, A. Eriksson, M. André, E. Engwall, Y. Wei, E. A. Kronberg, M. Fränz,
704 P. W. Daly, H. Zhao, and Q. Y. Ren, On the ionospheric source region of cold ion
705 outflow, *Geophys. Res. Lett.*, , 39, 18,102, 2012.
- 706 Li, K., S. Haaland, A. Eriksson, M. André, E. Engwall, Y. Wei, E. A. Kronberg, M. Fränz,
707 P. W. Daly, H. Zhao, and Q. Y. Ren, Transport of cold ions from the polar ionosphere
708 to the plasma sheet, *J. Geophys. Res.*, , 118, 5467–5477, 2013.
- 709 Lockwood, M., J. H. Waite, Jr., T. E. Moore, C. R. Chappell, and M. O. Chandler, The
710 cleft ion fountain, *J. Geophys. Res.*, , 90, 9736–9748, 1985a.
- 711 Lockwood, M., J. H. Waite, Jr., T. E. Moore, C. R. Chappell, and J. F. E. Johnson, A
712 new source of suprathermal O(+) ions near the dayside polar cap boundary, *J. Geophys.*
713 *Res.*, , 90, 4099–4116, 1985b.
- 714 Lybekk, B., A. Pedersen, S. Haaland, K. Svenes, A. N. Fazakerley, A. Masson, M. G. G. T.
715 Taylor, and J.-G. Trotignon, Solar cycle variations of the Cluster spacecraft potential
716 and its use for electron density estimations, *J. Geophys. Res.*, , 117, 1217, 2012.
- 717 Milan, S. E., Both solar wind-magnetosphere coupling and ring current intensity control
718 of the size of the auroral oval, *Geophys. Res. Lett.*, , 36, 18,101, 2009.
- 719 Moore, T., M. Chandler, C. Chappell, R. Comfort, P. Craven, D. Delcourt, H. Elliott,
720 B. Giles, J. Horwitz, C. Pollock, and Y.-J. Su, Polar/TIDE results on polar outflows,
721 in *Sun-Earth Plasma Connections*, edited by J. Burch and R.L.Carovillano, vol. 109 of
722 *Geophysical Monograph Series*, pp. 87–101, American Geophysical Union, 1999.
- 723 Moore, T. E., C. R. Chappell, M. O. Chandler, P. D. Craven, B. L. Giles, C. J. Pollock,
724 J. L. Burch, D. T. Young, J. H. Waite, Jr., J. E. Nordholt, M. F. Thomsen, D. J.

- 725 McComas, J. J. Berthelier, W. S. Williamson, R. Robson, and F. S. Mozer, High-
726 altitude observations of the polar wind., *Science*, *277*, 349–351, 1997.
- 727 Newell, P. T., and J. W. Gjerloev, SuperMAG-based partial ring current indices, *J. Geo-*
728 *phys. Res.*, , *117*, 5215, 2012.
- 729 Nilsson, H., M. Waara, O. Marghitsu, M. Yamauchi, R. Lundin, H. Rème, J.-A. Sauvaud,
730 I. Dandouras, E. Lucek, L. M. Kistler, B. Klecker, C. W. Carlson, M. B. Bavassano-
731 Cattaneo, and A. Korth, An assessment of the role of the centrifugal acceleration mech-
732 anism in high altitude polar cap oxygen ion outflow, *Annales Geophysicae*, *26*, 145–157,
733 2008.
- 734 Nilsson, H., E. Engwall, A. Eriksson, P. A. Puhl-Quinn, and S. Arvelius, Centrifugal
735 acceleration in the magnetotail lobes, *Annales Geophysicae*, *28*, 569–576, 2010.
- 736 Nilsson, H., I. A. Barghouthi, R. Slapak, A. I. Eriksson, and M. André, Hot and cold ion
737 outflow: Spatial distribution of ion heating, *J. Geophys. Res.*, , *117*, 11,201, 2012.
- 738 Paschmann, G., F. Melzner, R. Frenzel, H. Vaith, P. Parigger, U. Pagel, O. H. Bauer,
739 G. Haerendel, W. Baumjohann, N. Scopke, R. B. Torbert, B. Briggs, J. Chan, K. Lynch,
740 K. Morey, J. M. Quinn, D. Simpson, C. Young, C. E. McIlwain, W. Fillius, S. S. Kerr,
741 R. Mahieu, and E. C. Whipple, The Electron Drift Instrument for Cluster, *Space Sci.*
742 *Review*, *79*, 233–269, 1997.
- 743 Pedersen, A., P. Décréau, C. Escoubet, G. Gustafsson, H. Laakso, P. Lindqvist, B. Lybekk,
744 A. Masson, F. Mozer, and A. Vaivads, Four-point high time resolution information on
745 electron densities by the electric field experiments (EFW) on Cluster, *Ann. Geophys.*,
746 *19*, 1483–1489, 2001.

- 747 Pedersen, A., B. Lybekk, M. André, A. Eriksson, A. Masson, F. S. Mozer, P.-A.
748 Lindqvist, P. M. E. Décréau, I. Dandouras, J.-A. Sauvaud, A. Fazakerley, M. Taylor,
749 G. Paschmann, K. R. Svenes, K. Torkar, and E. Whipple, Electron density estimations
750 derived from spacecraft potential measurements on cluster in tenuous plasma regions,
751 *J. Geophys. Res.*, , 113, 2008.
- 752 Quinn, J. M., G. Paschmann, R. B. Torbert, H. Vaith, C. E. McIlwain, G. Haerendel,
753 O. Bauer, T. M. Bauer, W. Baumjohann, W. Fillius, M. Foerster, S. Frey, E. Georgescu,
754 S. S. Kerr, C. A. Kletzing, H. Matsui, P. Puhl-Quinn, and E. C. Whipple, Cluster EDI
755 convection measurements across the high-latitude plasma sheet boundary at midnight,
756 *Ann. Geophys.*, 19, 1669–1681, 2001.
- 757 Riedler, W., K. Torkar, F. Rudenauer, M. Fehringer, A. Pedersen, R. Schmidt, R. J. L.
758 Grard, H. Arends, B. T. Narheim, J. Troim, R. Torbert, R. C. Olsen, E. Whipple,
759 R. Goldstein, N. Valavanoglou, and H. Zhao, Active Spacecraft Potential Control, *Space*
760 *Sci. Review*, 79, 271–302, 1997.
- 761 Rodger, A. S., G. D. Wells, R. J. Moffett, and G. J. Bailey, The variability of Joule
762 heating, and its effects on the ionosphere and thermosphere, *Annales Geophysicae*, 19,
763 773–781, 2001.
- 764 Shelley, E. G., W. K. Peterson, A. G. Ghielmetti, and J. Geiss, The polar ionosphere as
765 a source of energetic magnetospheric plasma, *Geophys. Res. Lett.*, , 9, 941–944, 1982.
- 766 Sotirelis, T., P. T. Newell, and C. Meng, Shape of the open-closed boundary of the polar
767 cap as determined from observations of precipitating particles by up to four DMSP
768 satellites, *J. Geophys. Res.*, , 103, 399–406, 1998.

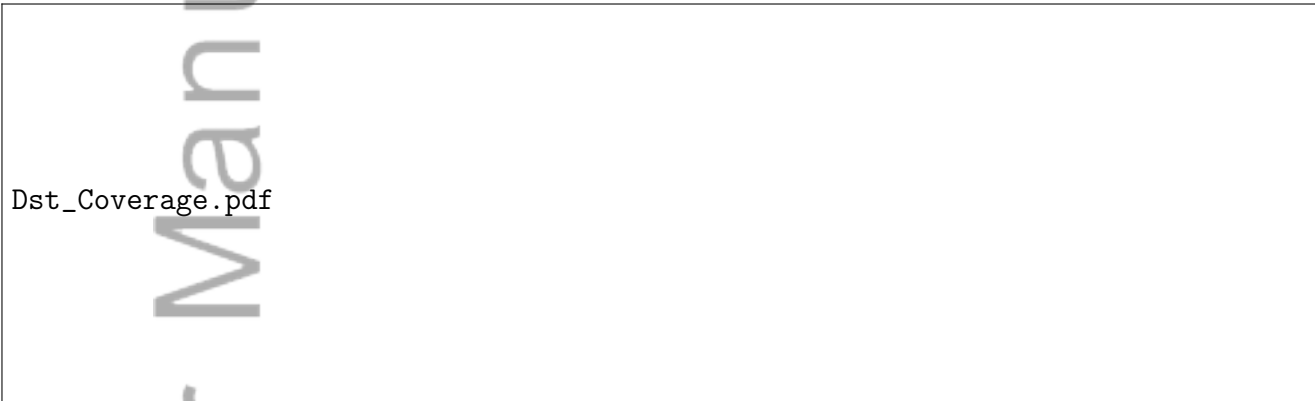
- 769 Strangeway, R. J., C. T. Russell, C. W. Carlson, J. P. McFadden, R. E. Ergun, M. Temerin,
770 D. M. Klumpar, W. K. Peterson, and T. E. Moore, Cusp field-aligned currents and ion
771 outflows, *J. Geophys. Res.*, , 2012.
- 772 Su, Y.-J., The photoelectron-driven polar wind: Coupled fluid- semikinetic simulations
773 and measurements by the thermal ion dynamics experiment on the POLAR spacecraft,
774 Ph.D. thesis, University of Alabama, Huntsville, 1998.
- 775 Su, Y.-J., J. L. Horwitz, T. E. Moore, B. L. Giles, M. O. Chandler, P. D. Craven, M. Hi-
776 rahara, and C. J. Pollock, Polar wind survey with the Thermal Ion Dynamics Ex-
777 periment/Plasma Source Instrument suite aboard POLAR, *J. Geophys. Res.*, , 103,
778 29,305–29,338, 1998.
- 779 Sugiura, M., Geomagnetic Storms, in *Natural Electromagnetic Phenomena*, edited by
780 D. F. Bleil, p. 49, 1964.
- 781 Svenes, K. R., B. Lybekk, A. Pedersen, and S. Haaland, Cluster observations of near-
782 Earth magnetospheric lobe plasma densities a statistical study, *Annales Geophysicae*,
783 26, 2845–2852, 2008.
- 784 Wahlund, J.-E., and H. J. Opgenoorth, EISCAT observations of strong ion outflows from
785 the F-region ionosphere during auroral activity - Preliminary results, *Geophys. Res.*
786 *Lett.*, , 16, 727–730, 1989.
- 787 Wahlund, J.-E., F. R. E. Forme, H. J. Opgenoorth, M. A. L. Persson, E. V. Mishin,
788 and A. S. Volokitin, Scattering of electromagnetic waves from a plasma - Enhanced ion
789 acoustic fluctuations due to ion-ion two-stream instabilities, *Geophys. Res. Lett.*, , 19,
790 1919–1922, 1992.

- 791 Wanliss, J. A., and K. M. Showalter, High-resolution global storm index: Dst versus
792 SYM-H, *J. Geophys. Res.*, , 111, 2202, 2006.
- 793 Whipple, E. C., J. M. Warnock, and R. H. Winkler, Effect of satellite potential on direct
794 ion density measurements through the plasmopause, *J. Geophys. Res.*, , 79, 179–186,
795 1974.
- 796 Wilson, G. R., D. M. Ober, G. A. Germany, and E. J. Lund, The relationship be-
797 tween suprathermal heavy ion outflow and auroral electron energy deposition: Po-
798 lar/Ultraviolet Imager and Fast Auroral Snapshot/Time-of-Flight Energy Angle Mass
799 Spectrometer observations, *J. Geophys. Res.*, , 106, 18,981–18,994, 2001.
- 800 Winsor, K. J., M. Lockwood, G. O. L. Jones, and P. J. S. Williams, Observations of
801 large field-aligned flows of thermal plasma in the auroral ionosphere, *Advances in Space*
802 *Research*, 9, 57–59, 1989.
- 803 Yau, A. W., and M. Andre, Sources of Ion Outflow in the High Latitude Ionosphere, *Space*
804 *Sci. Review*, 80, 1–25, 1997.
- 805 Yau, A. W., P. H. Beckwith, W. K. Peterson, and E. G. Shelley, Long-term (solar cy-
806 cle) and seasonal variations of upflowing ionospheric ion events at DE 1 altitudes, *J.*
807 *Geophys. Res.*, , 90, 6395–6407, 1985a.
- 808 Yau, A. W., L. Lenchyshyn, E. G. Shelley, and W. K. Peterson, Energetic auroral and
809 polar ion outflow at DE 1 altitudes Magnitude, composition, magnetic activity depen-
810 dence, and long-term variations, *J. Geophys. Res.*, , 90, 8417–8432, 1985b.
- 811 Yau, A. W., B. A. Whalen, C. Goodenough, E. Sagawa, and T. Mukai, EXOS D (Akebono)
812 observations of molecular NO(+) and N2(+) upflowing ions in the high-altitude auroral
813 ionosphere, *J. Geophys. Res.*, , 98, 11,205, 1993.

- 814 Yau, A. W., T. Abe, and W. K. Peterson, The polar wind: Recent observations, *Journal*
815 *of Atmospheric and Solar-Terrestrial Physics*, *69*, 1936–1983, 2007.
- 816 Zheng, Y., T. E. Moore, F. S. Mozer, C. T. Russell, and R. J. Strangeway, Polar study
817 of ionospheric ion outflow versus energy input, *J. Geophys. Res.*, , *110*, 7210, 2005.

Author Manuscript

Figure 1. Illustration of shielding due to spacecraft charging. Low energy ions emanating from the polar cap region travel upwards along the magnetic field lines. Due to positive spacecraft charging, ions with energies below the spacecraft potential energy will not reach particle detectors onboard the satellite - they remain 'invisible'. A wake will be formed downstream of the spacecraft.



Dst_Coverage.pdf

Figure 2. Plot of the SMR (Dst) index for 2001-2010. Red color indicates periods where cold ion observations are available from Cluster. Measurements are only possible when Cluster has apogee in the tail during late July to early November. To be useful for our statistics, we require coverage for at least parts of the main phase and parts of the recovery phase of a storm. These criteria are fulfilled for 32 storms (see Appendix 5). The two GEM events in October 2002, discussed in some detail in the present paper are indicated by blue bars.

Dst_Generic_GEMstorms.pdf

Figure 3. Panel a) Characteristic phases of a geomagnetic storm as manifested in the SMR index. The numbered labels indicate stages of evolution and will be used to parametrize a model of the cold ion outflow for a characteristic storm. For comparison, we also show the SMR index for each of the geomagnetic storms on 1-5 October 2002 (panel b) and 23-28 October 2004 (panel c), respectively, selected by the GEM community for modelling and benchmarking. Red bars indicate intervals where cold ion measurements are available. To guide the reader, dashed gray lines repeat the time profile of the generic storm.



Figure 4. Key observations for the two GEM storm intervals discussed in this paper. Left panels: Detailed observations for event 1 - the geomagnetic storm on 30 September - 5 October 2002. Right panels: Same as left panels, but for event 2 - the geomagnetic storm on 23 - 28 October 2002. To facilitate comparison, vertical axis scales are the same as for event 1. Panels show: a) XZ_{GSE} projection of the Cluster orbit; b) SMR (Dst) index; c) Size of source area; d) F10.7 index; e) Solar wind dynamic pressure; f) Cold ion density; g) Outflow bulk velocity; h) Calculated ionospheric flux; i) Convection velocity.

A	B	C	D	E	F	G	H	I	J
Storm phase	Num records	Period with data available	$\langle Dst \rangle$ [nT]	$\langle Ne \rangle$ [cm^{-3}]	$\langle V_{ } \rangle$ [kms^{-1}]	$\langle Flux \rangle$ [$10^8 cm^{-2} s^{-1}$]	PC area [$10^7 km^2$]	Outflow rate [$10^{26} s^{-1}$]	$\langle V_{\perp} \rangle$ [kms^{-1}]
③ Peak	575	02 Oct, 01:01-04:04	-149.0	0.88	21.0	3.06	7.44	2.22	12.9
④ Recovery	2310	04 Oct, 10:10-22:10	-95.0	0.23	27.2	2.49	5.02	1.31	17.6

Table 1. Summary of cold ion observations during the first GEM storm on 1-5 October 2002. Observations were only available during the peak (i.e., SMR (Dst) \leq -135 nT) and the recovery phase of the storm. The notation $\langle \rangle$ indicate median values of the respective parameter. The source area in column H is the combined area of northern and southern hemispheres.

A	B	C	D	E	F	G	H	I	J
Storm phase	Num records	Period with data available	$\langle Dst \rangle$ [nT]	$\langle Ne \rangle$ [cm^{-3}]	$\langle V_{ } \rangle$ [kms^{-1}]	$\langle Flux \rangle$ [$10^8 cm^{-2} s^{-1}$]	PC area [$10^7 km^2$]	Outflow rate [$10^{26} s^{-1}$]	$\langle V_{\perp} \rangle$ [kms^{-1}]
① Initial	1853	23 Oct, 11:11-22:10	-20.0	0.08	23.2	0.89	2.97	0.35	10.1
② Main	128	24 Oct, 06:06-23:11	-70.0	0.08	42.3	1.88	4.32	0.72	16.9
③ Peak	1523	24 Oct, 16:04-25, 09:09	-84.0	0.13	28.4	2.12	4.89	0.97	17.6
④ Recovery	2589	(24 Oct, 20:08-23:11)	-78.0	0.15	27.4	1.49	4.30	0.72	15.4

Table 2. As Table 1 but for the GEM storm on 23-28 Oct 2002.

A	B	C	D	E	F	G	H	I	J
Storm phase	Number of records	$\langle Duration \rangle$ [hours]	$\langle Dst \rangle$ [nT]	$\langle Ne \rangle$ [cm^{-3}]	$\langle V_{ } \rangle$ [kms^{-1}]	$\langle Flux \rangle$ [$10^8 cm^{-2} s^{-1}$]	PC area [$10^7 km^2$]	Outflow rate [$10^{26} s^{-1}$]	$\langle V_{\perp} \rangle$ [kms^{-1}]
Non-storm	10824	-	6.0	0.13	19.2	1.27	2.61	0.33	8.9
① Initial/SSC	10356	4.0	-7.0	0.13	22.7	3.35	2.98	0.52	11.1
② Main	18771	5.0	-39.0	0.34	29.2	3.35	4.38	1.66	14.3
ⓐ - early	7801	-	-17.0	0.23	27.9	2.26	3.81	0.88	14.3
ⓑ - late	10970	-	-48.0	0.43	30.1	4.58	4.65	3.08	14.3
③ Peak	21535	12.0	-65.0	0.42	36.7	5.31	4.50	2.73	16.3
④ Recovery	110815	84.0	-34.0	0.11	25.3	1.58	3.56	0.58	12.9
ⓐ - early	52748	-	-60.0	0.15	27.6	2.33	3.92	0.98	15.1
ⓑ - late	58067	-	-18.0	0.08	23.0	1.19	3.10	0.36	10.7

Table 3. Similar to Tables 1 and 2, but now with characteristics for the full dataset.

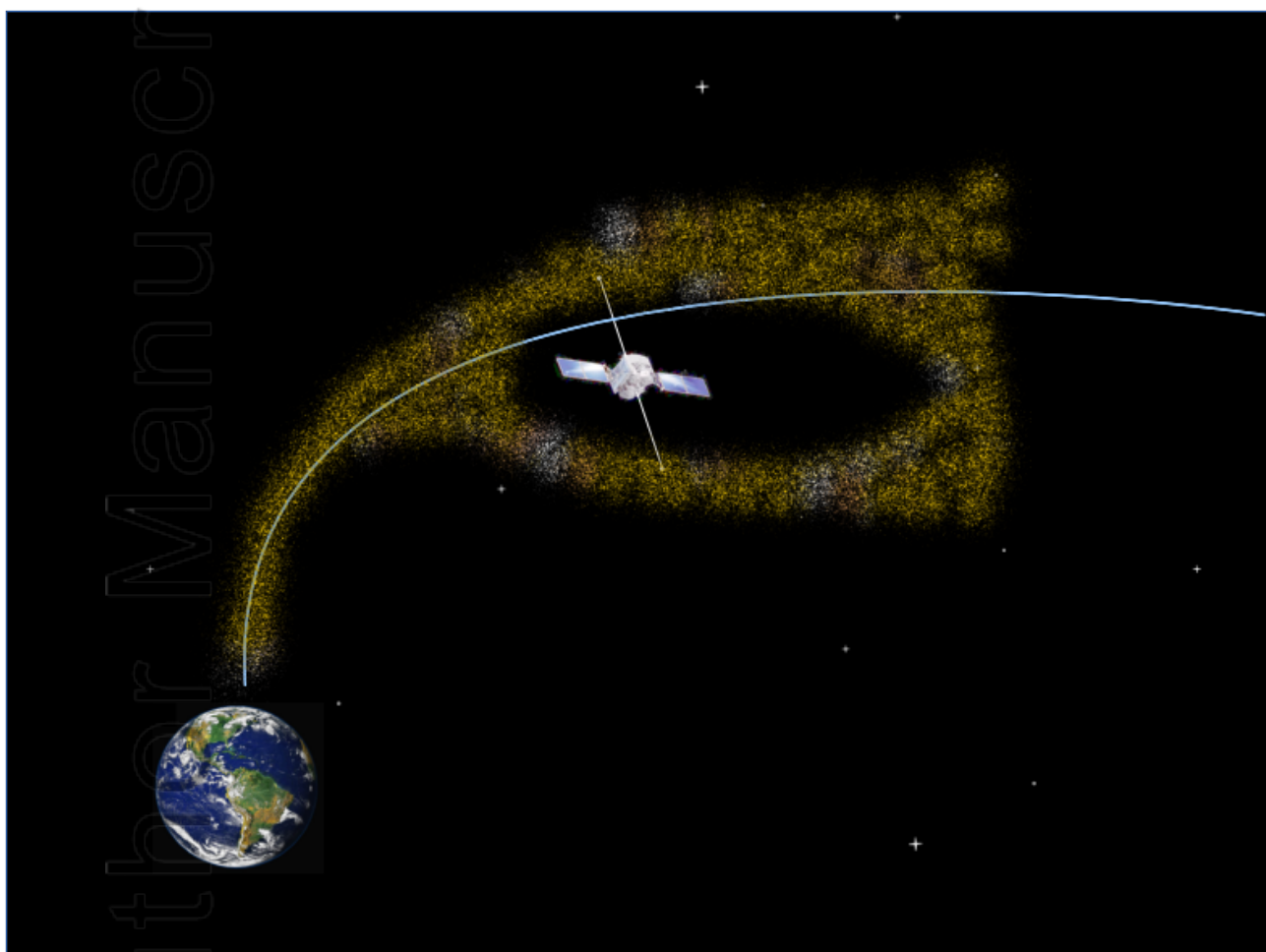
Rather than individual times, we now provide the average duration of the various stages of storm evolution in column C. Not all storms had a pronounced initial phase or storm sudden commencement, so estimates for this phase are less reliable. This table defines our “generic storm”.

Figure 5. Illustration of orbital bias. Recall that wake measurements are only available in the high latitude, nightside lobe regions. Due to the evolution of Cluster’s orbit (blue dashed line), with apogee moving further into the southern lobe as the years pass, we are more likely to observe outflow from a given source location in the ionosphere during quiet periods (blue transport path) in the southern hemisphere and in the northern hemisphere during disturbed periods (fast convection, orange outflow transport path).

Year	Storm interval	SMR_{min}
2001	19 Aug 15:07 - 21 Aug 11:07	-133
2001	13 Sep 13:21 - 14 Sep 02:21	-58
2001	23 Sep 13:51 - 25 Sep 16:51	-83
2001	28 Sep 07:13 - 30 Sep 13:13	-116
2001	3 Oct 02:25 - 4 Oct 19:25	-122
2001	5 Oct 11:36 - 7 Oct 07:36	-184
2001	11 Oct 21:02 - 12 Oct 00:02	-73
2001	12 Oct 05:38 - 14 Oct 07:38	-79
2001	24 Oct 12:39 - 26 Oct 19:39	-211
2001	28 Oct 03:43 - 30 Oct 19:43	-140
2002	5 Jul 17:36 - 8 Jul 10:36	-54
2002	12 Jul 21:24 - 14 Jul 20:24	-48
2002	1 Aug 10:11 - 1 Aug 18:11	-52
2002	2 Aug 23:11 - 3 Aug 20:11	-78
2002	4 Aug 03:46 - 5 Aug 02:46	-49
2002	19 Aug 23:06 - 23 Aug 23:06	-96
2002	10 Sep 16:18 - 18 Sep 07:18	-166
2002	4 Oct 10:45 - 13 Oct 15:45	-181
2002	14 Oct 05:09 - 15 Oct 11:09	-94
2002	15 Oct 16:30 - 16 Oct 14:30	-46
2002	24 Oct 06:31 - 29 Oct 02:31	-85
2002	28 Oct 05:01 - 30 Oct 03:01	-48
2003	12 Jul 15:04 - 14 Jul 15:04	-108
2003	17 Jul 03:28 - 19 Jul 09:28	-106
2003	26 Jul 18:02 - 27 Jul 17:02	-62
2003	6 Aug 12:19 - 7 Aug 16:19	-63
2003	19 Aug 09:20 - 21 Aug 06:20	-148
2003	21 Aug 04:43 - 25 Aug 10:43	-59
2003	24 Sep 00:40 - 27 Sep 14:40	-48
2003	2 Oct 16:15 - 4 Oct 20:15	-52
2003	17 Oct 18:58 - 20 Oct 14:58	-103
2003	30 Oct 19:23 - 3 Nov 00:23	-409
2004	16 Jul 22:53 - 19 Jul 10:53	-96
2004	22 Jul 21:19 - 23 Jul 18:19	-104
2004	25 Jul 22:45 - 26 Jul 23:45	-149
2004	28 Jul 02:23 - 31 Jul 04:23	-234
2004	3 Sep 20:13 - 7 Sep 09:13	-133
2004	20 Oct 03:46 - 22 Oct 15:46	-47
2005	9 Jul 10:52 - 10 Jul 02:52	-57
2005	29 Jul 23:03 - 1 Aug 05:03	-45
2005	11 Sep 13:32 - 15 Sep 08:32	-132
2006	5 Jul 16:13 - 9 Jul 22:13	-50
2006	29 Jul 12:09 - 31 Jul 17:09	-59
2006	7 Aug 23:38 - 11 Aug 01:38	-53
2006	19 Aug 13:21 - 24 Aug 02:21	-83
2006	5 Sep 19:31 - 10 Sep 00:31	-56
2006	30 Sep 18:05 - 4 Oct 09:05	-49
2007	14 Jul 10:40 - 17 Jul 14:40	-48
2009	23 Oct 17:41 - 25 Oct 00:41	-46
2010	6 Aug 11:21 - 9 Aug 12:21	-79

Table 4. List of storms used to generate our characteristic storm described in Section 3.3 and Table 3.

Author Manuscript



2015JA021810-f01-z-.png

